The Astrophysical Journal, 997:217 (12pp), 2026 February 1 https://doi.org/10.3847/1538-4357/ae2257
© 2026. The Author(s). Published by the American Astronomical Society.
OPEN ACCESS

Evidence of an Energetic Magnetar Powering 1LHAASO J0500+4454

J. A. J. Alford[1,3], J. D. Gelfand[1,3], M. Abdelmaguid[1,3], and P. Slane[2]
[1] Division of Science, New York University Abu Dhabi, PO Box 129188, Abu Dhabi, UAE; alford@nyu.edu
[2] Harvard-Smithsonian Center for Astrophysics, 60 Garden Street, Cambridge, MA 02138, USA
[3] Center for Astrophysics and Space Science (CASS), New York University Abu Dhabi, PO Box 129188, Abu Dhabi, UAE
Received 2025 March 3; revised 2025 November 18; accepted 2025 November 18; published 2026 January 23

Abstract

We investigate the origin of the unidentified, extended TeV source 1LHAASO J0500+4454, considering three possible origins: cosmic rays interacting with a molecular cloud (MC), particles accelerated in a currently undetected supernova remnant (SNR), and an energetic outflow powered by a pulsar. Upper limits on the CO and X-ray emission from the γ-ray emitting region disfavor the MC and SNR scenarios, respectively. If a nebula of inverse Compton scattering $e^{\pm}$powers 1LHAASO J0500+4454, then spectral energy distribution modeling indicates that the current particle energy in the nebula is $\sim 4 \times 10^{48}$ erg. If the coincident magnetar SGR 0501+4516's rotational energy powered 1LHAASO J0500+4454, then a conservative energy budget calculation requires an initial magnetar spin period $P_0 \lesssim 5$ ms and a spin-down timescale $\tau_{sd} \lesssim 30$ yr, which has implications for the origins of magnetars.

Unified Astronomy Thesaurus concepts: Gamma-ray sources (633); Magnetars (992); Pulsar wind nebulae (2215); Pulsars (1306); Supernovae (1668)

1. Introduction

Surveys of the γ-ray sky are pushing the frontier to higher photon energies and discovering lower surface brightness γ-ray sources. Recently, Z. Cao et al. (2024) published the 1LHAASO catalog of 90 very-high-energy (VHE, $E > 0.1$ TeV) γ-ray sources. At least 35 1LHAASO sources are associated with pulsars and pulsar wind nebulae (PWNe). 1LHAASO J0500+4454 is one of 15 unidentified TeV sources in the 1LHAASO catalog, and is located toward the relatively uncrowded Galactic anticenter region, where it may be easier to identify its origin. Within 1LHAASO J0500+4454's $\theta_\gamma = 0.^\circ41 \pm 0.^\circ07$ radial extent lies the (also unidentified) Fermi source 4FGL J0501.7+4459 (J. Ballet et al. 2023).

Identifying the origins of γ-ray sources requires distinguishing between "leptonic" or "hadronic" γ-ray production, according to the classification of the particles producing the majority of the γ-rays. In the hadronic scenario, high-energy protons collide with other protons in a dense medium (e.g., a molecular cloud, MC) to produce neutral pions (π^0), which then decay into the observed γ-rays. High-energy p^+ are believed to be accelerated in SNRs, so MCs near SNRs are prime candidates for producing γ-ray sources (M. Ackermann et al. 2013; F. A. Aharonian 2013). In the leptonic scenario, high-energy $e^{\pm}$ produce γ-rays through inverse Compton scattering photons from the cosmic microwave background (CMB) and other photon fields. High-energy $e^{\pm}$ are produced in SNRs, pulsar magnetospheres, and at the termination shocks of PWNe, so both SNRs and pulsars are plausible sources of leptonic γ-rays.

The magnetar SGR 0501+4516 is the only known pulsar located within the extent of 1LHAASO J0500+4454 (see Figure 1), raising the possibility of a physical association. Unlike rotationally powered pulsars, magnetars are not often associated with extended VHE γ-ray sources, though some associations have been proposed (J. P. Halpern & E. V. Gotthelf 2010; H. E. S. S. Collaboration et al. 2018; E. V. Gotthelf et al. 2019), and young magnetars might have sufficient rotational and/or magnetic energy budgets (R. C. Duncan & C. Thompson 1992; A. M. Beloborodov & X. Li 2016; V. M. Kaspi & A. M. Beloborodov 2017). SGR 0501+4516's spin parameters and associated physical properties are listed in Table 1. No known SNRs or dense molecular clouds overlap 1LHAASO J0500+4454.

This paper is organized as follows: Section 2 outlines the basic physical properties of 1LHAASO J0500+4454 and its environment. Section 3 presents leptonic and hadronic models of the spectral energy distribution (SED) of 1LHAASO J0500+454 and the associated Fermi source. Section 4 investigates possible origins of 1LHAASO J0500+4454 and finds evidence for a PWN origin. Section 5 discusses the PWN energy budget if 1LHAASO J0500+4454 is a magnetar-powered PWN. Section 6 discusses our results in relation to previous work and discusses the implications of magnetar TeV emission for magnetar birth properties and origins.

2. Physical Properties of the 1LHAASO J0500+4454 Region

2.1. Distance and Environment

1LHAASO J0500+4454 is located at R.A. $= 75.^\circ01$, decl. $= 44.^\circ92$ ($l = 161.^\circ71$, $b = 1.^\circ58$), toward the Galactic anticenter region and $1.^\circ6$ above the Galactic plane, implying a distance of $D_\gamma \sim 2$ kpc if located in the Perseus Arm of the Milky Way (Y. Xu et al. 2006). 1LHAASO J0500+4454's radial extent $\theta_\gamma = 0.^\circ41 \pm 0.^\circ07$ corresponds to a physical radius

$$R_\gamma = 14.3^{+2.4}_{-2.4} \left(\frac{D_\gamma}{2\ \mathrm{kpc}}\right) \ \mathrm{pc}. \quad (1)$$

Figure 1 shows the position of 1LHAASO J0500+4454 in relation to all pulsars, SNRs, and Fermi sources listed in the ATNF Pulsar Catalog (version 2.1.1), Green's SNR catalog, and Fermi LAT 14 yr Source Catalog (4FGL-DR4), respectively (R. N. Manchester et al. 2005;

Original content from this work may be used under the terms of the Creative Commons Attribution 4.0 licence. Any further distribution of this work must maintain attribution to the author(s) and the title of the work, journal citation and DOI.

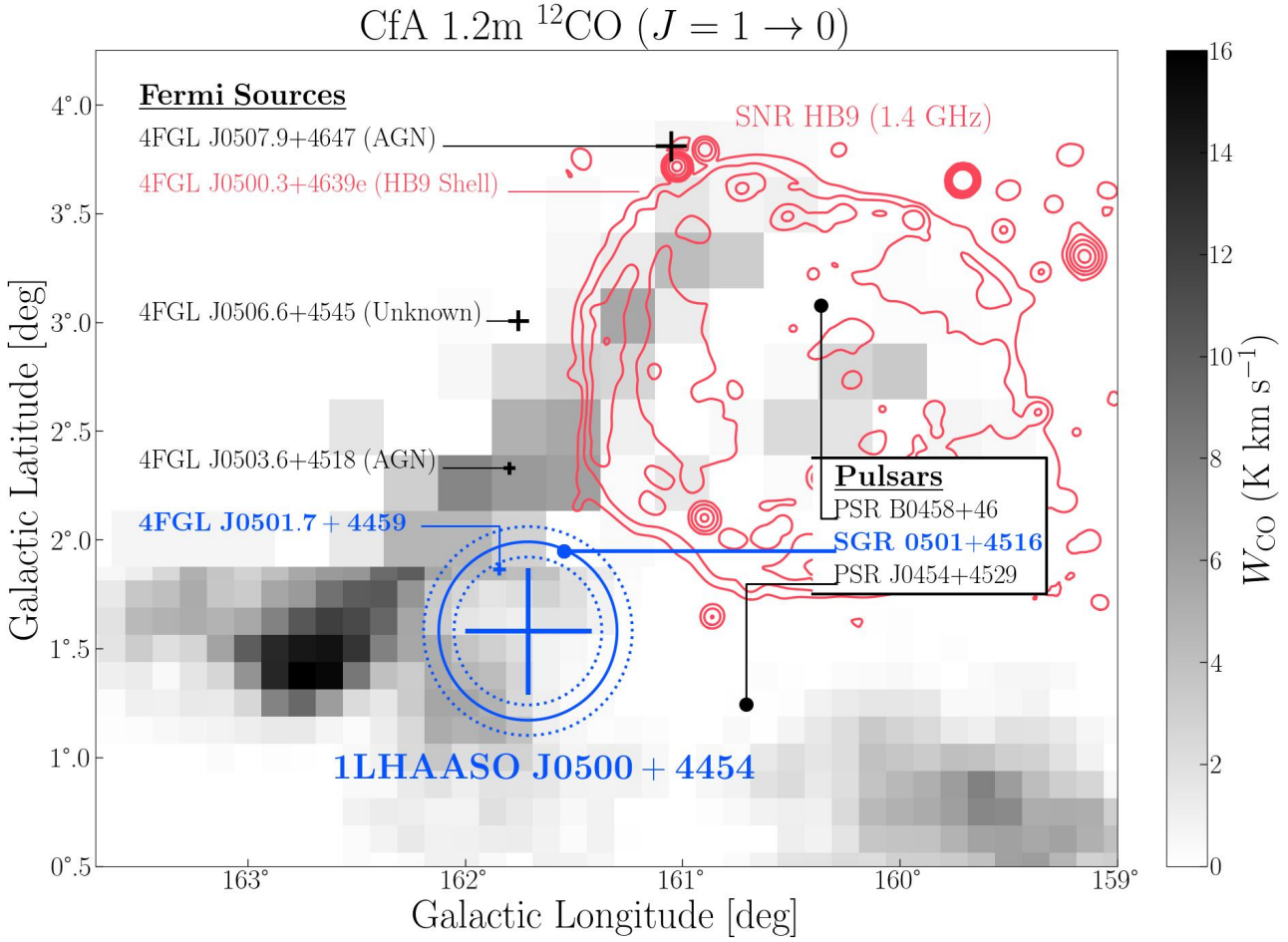

Figure 1. ^{12}CO ($J = 1 \rightarrow 0$) map of the region around 1LHAASO J0500+4454, integrated in the velocity range −7.15 to 4.55 km s^{-1}. The solid blue circle indicates the angular extent of 1LHAASO J0500+4454, $\theta_\gamma = 0.^\circ41 \pm 0.^\circ07$, and the dotted blue circles indicate the uncertainty in R_γ. The blue crosshairs indicate the positional uncertainty of 1LHAASO J0500+4454 at the 95% confidence level. Black crosshairs indicate the positions (at 95% confidence) of Fermi 4FGL-DR4 sources in the field, and associations listed in the Fermi 4FGL-DR4 catalog are indicated in parentheses. All known pulsars and SNRs in the field are indicated. Red contours trace the 1.4 GHz radio shell of the supernova remnant HB9.

Table 1
Known Pulsars Near 1LHAASO J0500+4454

Pulsar	P (s)	$\dot{P}$ (10^{-15} s s^{-1})	$\dot{E}$ (10^{31} erg s^{-1})	τ_{char} (kyr)	B_s (10^{12} G)	References
SGR 0501+4516	≈5.76	≈5900	120	15	190	(1)
PSR J0454+4529	≈1.39	≈4.9	7.8	4500	2.5	(2)
PSR B0458+46	≈0.64	≈5.6	84	1800	1.1	(3)

References. (1) A. Camero et al. (2014), (2) C. M. Tan et al. (2020), (3) G. Hobbs et al. (2004)

D. A. Green 2019, 2025; J. Ballet et al. 2023). SGR 0501 +4516 is the only pulsar coincident with 1LHAASO J0500 +4454. Y.-L. Mong & C.-Y. Ng (2018) measured an upper limit on SGR 0501+4516's proper motion that ruled out an association with the SNR HB9. Recently, A. A. Chrimes et al. (2025) measured $\mu = 5.4$ mas yr^{-1}, implying that SGR 0501+4516's birth site overlaps 1LHAASO J0500 +4454, if SGR 0501+4516's true age is comparable to its characteristic age ($\tau_{char} = 15$ kyr).

Figure 1 also shows the ^{12}CO ($J = 1 \rightarrow 0$) luminosity L_{co} in the region surrounding 1LHAASO J0500+4454 (T. M. Dame & P. Thaddeus 2022). Carbon monoxide (CO) emission traces molecular material (P. Thaddeus 1977), and Figure 1 demonstrates that there is some molecular material coincident with 1LHAASO J0500+4454. We calculate an upper limit on the molecular density within the 1LHAASO J0500+4454 region by assuming that all of the observed CO intensity W_{co} is emitted from a hypothetical spherical cloud centered on the γ-ray source. We integrate W_{co} within the $\theta_\gamma = 0.^\circ41$ extent of 1LHAASO J0500 +4454 and the velocity range $-7.15\,\mathrm{km\,s^{-1}} < V_{LSR} < 4.55\,\mathrm{km\,s^{-1}}$ (there is no significant CO emission within 1LHAASO J0500+4454 at other

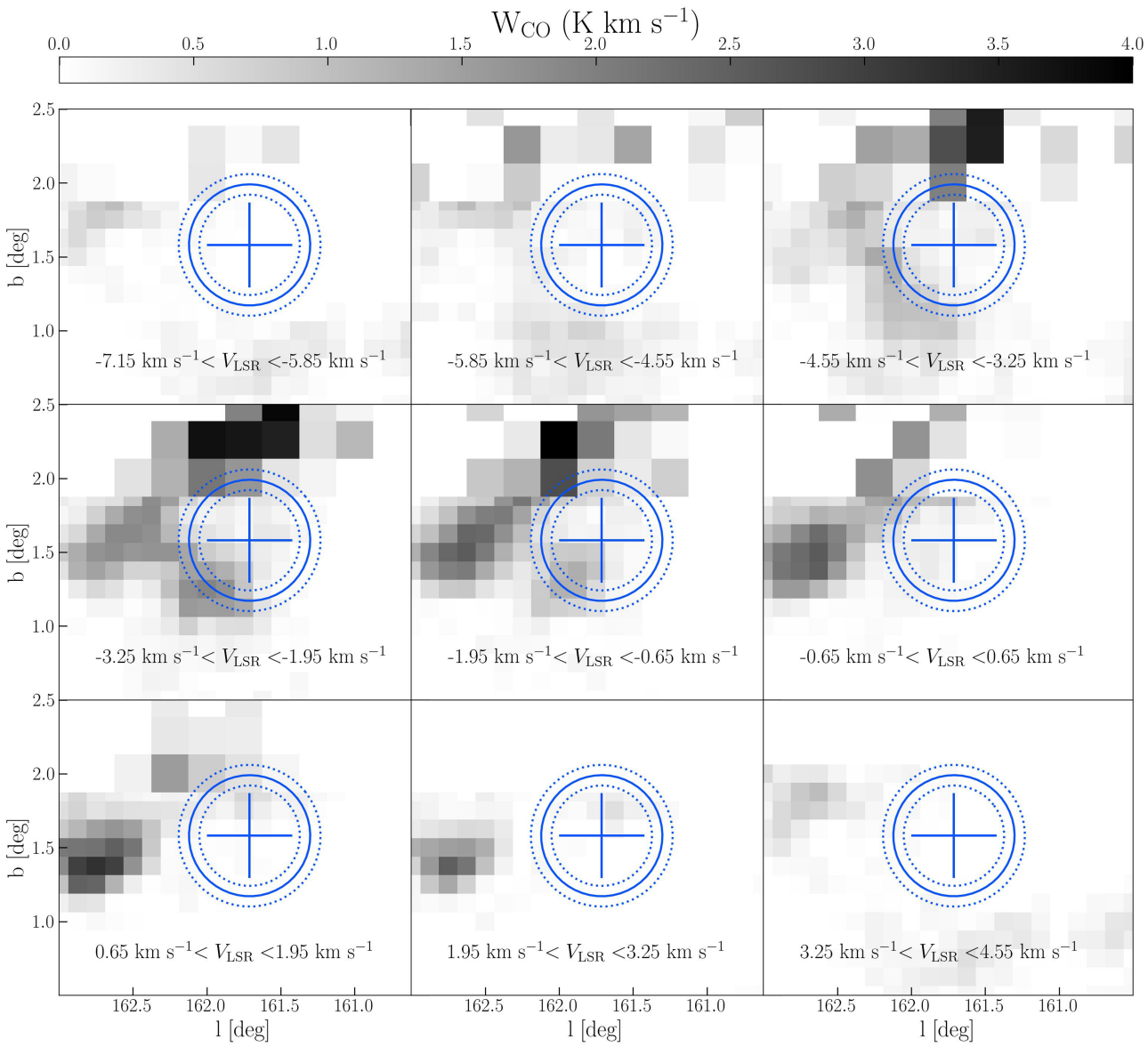

Figure 2. ^{12}CO ($J = 1 \rightarrow 0$) maps of the region around 1LHAASO J0500+4454, integrated in various velocity ranges. The solid blue circle indicates the angular extent of 1LHAASO J0500+4454 $\theta_\gamma = 0.^\circ41 \pm 0.^\circ07$, and the dotted blue circles indicate the uncertainty in θ_γ. The blue crosshairs indicate the positional uncertainty of 1LHAASO J0500+4454 at the 95% confidence level.

velocities covered in the CfA CO survey data), and find

$$\int W_{\rm co} d\Omega = 0.82 \text{ K km s}^{-1} \text{ deg}^2. \quad (2)$$

We convert the observed CO luminosity to an upper limit on a molecular cloud mass using a CO-to-H2 conversion factor of 2×10^{20} cm^{-2}(K km s^{-1})$^{-1}$, which includes a factor of 1.36 to account for heavy elements (A. D. Bolatto et al. 2013; T. M. Dame & P. Thaddeus 2022):

$$M_{\rm cloud} \lesssim 4300 \left(\frac{\int W_{\rm co} d\Omega}{0.82 \text{ K km s}^{-1} \text{ deg}^2} \right) \times \left(\frac{D_\gamma}{2 \text{ kpc}} \right)^2 M_\odot. \quad (3)$$

The upper limit on proton number density $n_{\rm cloud}$ of this hypothetical spherical cloud with mass $M_{\rm cloud}$ and radius R_γ is:

$$n_{\rm cloud} \lesssim \left(\frac{M_{\rm cloud}}{\frac{4}{3}\pi R_\gamma^3} \right) m_{p^+}^{-1} \approx 14 \pm 7 \left(\frac{D_\gamma}{2 \text{ kpc}} \right)^{-1} \text{ cm}^{-3}. \quad (4)$$

Figure 1 suggests that there is a shell of CO emission coincident with the boundary of 1LHAASO J0500+4454 and spanning velocities $-4.55 \text{ km s}^{-1} < V_{\rm LSR} < 0.65 \text{ km s}^{-1}$. Figure 2 shows this same CO data in specific velocity ranges, so that the CO emission within 1LHAASO J0500 +4454 is more easily seen (note the change in scale in Figure 1 versus Figure 2). The $\approx 14 \text{ cm}^{-3}$ cloud density estimated above is a conservative upper limit of the actual H density within 1LHAASO J0500+4454, because it is the velocity-integrated value.

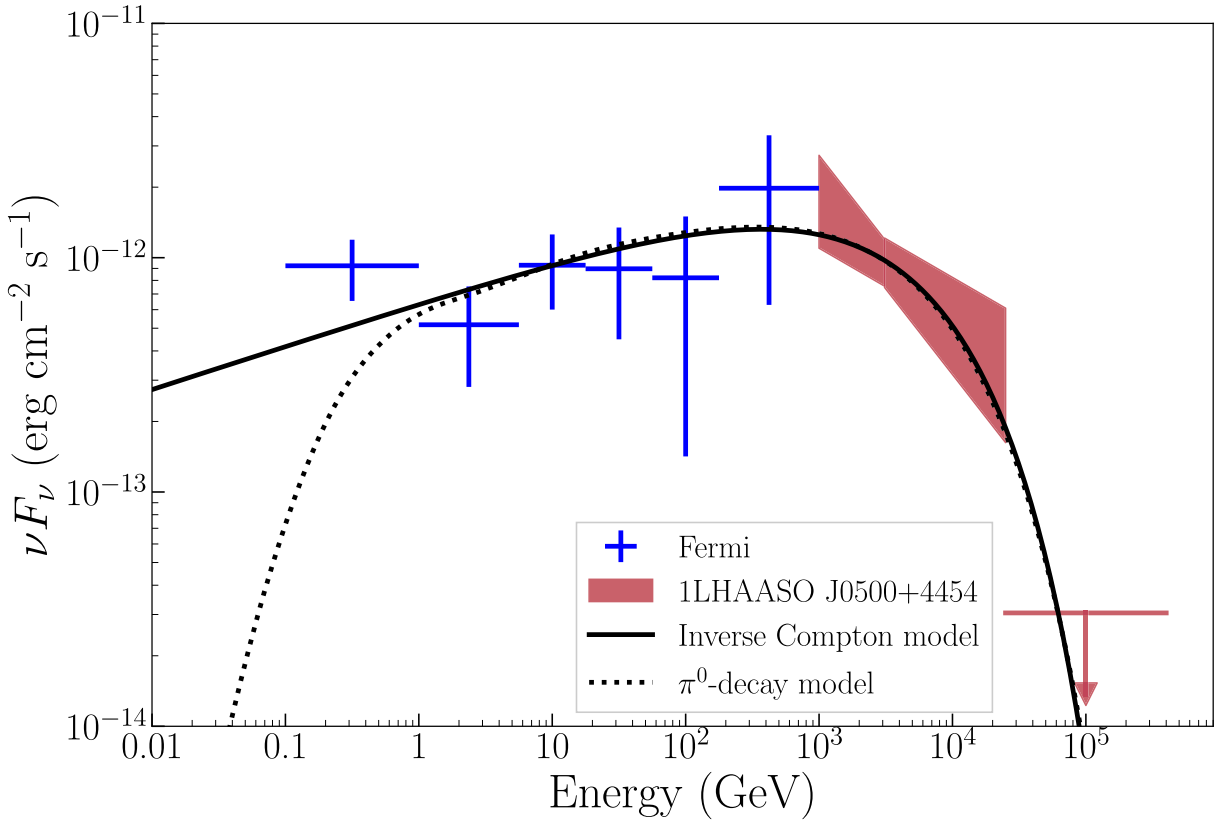

Figure 3. Combined SED of 1LHAASO J0500+4454 and the associated Fermi source. The solid curve shows the SED predicted by an inverse Compton (IC) model from an exponentially cutoff power-law electron population upscattering CMB photons. The dashed curve shows the π^0-decay model.

2.2. Fermi LAT Analysis and γ-ray SED

We selected photons within a 20° radius centered on 1LHAASO J0500 +4454 (R.A. = 75.°04, decl. = 44.°91), with photon energies ranging from 100 MeV to 500 GeV, and zenith angles less than 90°. The data were binned to 0.°05 per pixel. We used the `gill_iem_v07` and `iso_P8R3_SOURCE_V3_v1` templates to model the Galactic diffuse and isotropic backgrounds, respectively. We first fit the Fermi LAT 14 yr Source Catalog (4FGL-DR4) to the data, and then refit after removing 4FGL-DR4 point source 4FGL J0501.7 +4459 and replacing it with a source with the same position and extension as 1LHAASO J0500+4454. We find a 3σ preference for the later, extended morphology of 1LHAASO J0500+4454. Figure 3 shows the SED of this Fermi source.

Figure 3 also shows the 1LHAASO J0500+4454 SED. We obtained the 1LHAASO J0500+4454 SED data from the First LHAASO Catalog of Gamma-Ray Sources, Z. Cao et al. (2024). The 1LHAASO J0500+4454 SED in the 1–25 TeV band is a power law $\frac{dN}{dE} = N_0\left(\frac{E}{3\ \mathrm{TeV}}\right)^{-\Gamma}$ with $N_0 = 0.69 \pm 0.16 \times 10^{-13}\,\mathrm{cm^{-2}\,s^{-1}\,TeV^{-1}}$ and $\Gamma = 2.53 \pm 0.20$. 1LHAASO J0500+4454 was not detected above 25 TeV, with an upper limit $N_0 < 0.09 \times 10^{-16}\,\mathrm{cm^{-2}\,s^{-1}\,TeV^{-1}}$ calculated for a source with the same radius, position, and power-law spectrum $\frac{dN}{dE} = N_0\left(\frac{E}{50\ \mathrm{TeV}}\right)^{-2.53}$.

2.3. Leptonic Cooling Timescales

If the LHAASO TeV and Fermi GeV emission is leptonic, produced by $e^{\pm}$ inverse Compton scattering CMB photons, then the observed IC photon energies E_γ correspond to $e^{\pm}$ energies $E_{e^{\pm}}$ through the relation (G. B. Rybicki & A. P. Lightman 1979):

$$E_{e^{\pm}} \approx 63 \sqrt{\frac{E_\gamma}{10\ \ \mathrm{TeV}}}\ \mathrm{TeV}. \tag{5}$$

Equation (5) indicates that the LHAASO observed photon energy range $1\ \mathrm{TeV} \leqslant E_\gamma \leqslant 25\ \mathrm{TeV}$ corresponds to an $e^{\pm}$ energy range $20\ \mathrm{TeV} \lesssim E_{e^{\pm}} \lesssim 100\ \mathrm{TeV}$. The $e^{\pm}$ will lose energy through both inverse Compton scattering and synchrotron radiation. Assuming the CMB dominates the photon energy density, an e^- of energy 40 TeV upscattering CMB photons will lose half its energy on an inverse Compton cooling timescale

$$\tau_{\mathrm{IC}} \approx 30\left(\frac{E_{e^{\pm}}}{40\ \mathrm{TeV}}\right)^{-1}\ \mathrm{kyr}, \tag{6}$$

and on a synchrotron cooling timescale

$$\tau_{\mathrm{sync}} \approx 50\left(\frac{E_{e^{\pm}}}{40\mathrm{TeV}}\right)^{-1}\left(\frac{B_\perp}{2\mu\mathrm{G}}\right)^{-2}\ \mathrm{kyr}. \tag{7}$$

τ_{sync} is less certain than τ_{IC} because of its $\tau_{\mathrm{sync}} \propto B_\perp^{-2}$ dependence. We therefore adopt $\tau_{\mathrm{IC}} \approx 30$ kyr as a conservative upper limit on the age of γ-ray emitting $e^{\pm}$ in 1LHAASO J0500+4454.

3. SED Modeling

We modeled the SED of 1LHAASO J0500+4454 (presented in Section 2.2) in order to calculate W, the total particle energy in this TeV source. We performed this SED

Table 2
SED Modeling Results

Model	$\frac{dN}{dE}$	A (eV^{-1})	α	$E_{\rm cut}$ (TeV)	χ^2_ν (d.o.f.)
Leptonic (Inverse Compton)	$A\left(\frac{E_{e^\pm}}{1\,\mathrm{TeV}}\right)^{-\alpha}\exp\left(\frac{-E_{e^\pm}}{E_{\rm cut}}\right)$	$(1.95 \pm 0.27) \times 10^{34}$	2.63 ± 0.08	37 ± 7	0.6 (9)
Hadronic (π^0-decay)	$A\left(\frac{E_{p^+}}{1\,\mathrm{TeV}}\right)^{-\alpha}\exp\left(\frac{-E_{p^+}}{E_{\rm cut}}\right)$	$(8.9 \pm 1.4) \times 10^{34}$	1.91 ± 0.07	70 ± 19	0.9 (9)

Note. Results of fitting leptonic and hadronic SED models to the γ-ray emission from the 1LHAASO J0500+4454 region, including data from Fermi LAT, LHAASO WCDA, and LHAASO KM2A detectors (Figure 3). The leptonic and hadronic models are powered by exponentially cutoff power-law particle distributions $\frac{dN}{dE}$. 1σ errors on the model parameters are indicated.

modeling using `Naima` (V. Zabalza 2015). Section 3.1 discusses the leptonic model, and Section 3.2 discusses the hadronic model.

3.1. Leptonic (IC) Model

We fit the combined Fermi LAT and 1LHAASO J0500+4454 SED with an inverse Compton emission model where relativistic $e^\pm$ upscatter CMB seed photons. We explored both pure power law and exponentially cutoff power law particle spectra, and found that an exponentially cutoff power law

$$\frac{dN}{dE} = A\left(\frac{E_{e^\pm}}{1\,\mathrm{TeV}}\right)^{-\alpha}\exp\left(\frac{-E_{e^\pm}}{E_{\rm cut}}\right)\ \mathrm{eV}^{-1} \quad (8)$$

is required to fit the data. The best fit parameters are listed in Table 2, with 1σ errors computed from the covariance matrix. Figure 3 shows the SED predicted by this model and the observed SED. We calculate the total $e^\pm$ energy $W_{e^\pm}$ ($\equiv\int_{E_{\rm min}}^{E_{\rm max}} E_{e^\pm}\frac{dN}{dE}dE_{e^\pm}$) by setting $E_{\rm max} = 510$ TeV (the `Naima` default value and $\gg E_{\rm cut}$) and leaving $E_{\rm min}$ as a free parameter:

$$W_{e^\pm} \approx 3.8^{+2.7}_{-1.6} \times 10^{48}\left(\frac{E_{\rm min}}{1\,\mathrm{GeV}}\right)^{2-\alpha}\left(\frac{D_\gamma}{2\,\mathrm{kpc}}\right)^2\ \mathrm{erg}. \quad (9)$$

The 1σ errors in $W_{e^\pm}$ (and in W_{p^+} below) were computed by Monte Carlo sampling. The total number of particles N ($\equiv\int_{E_{\rm min}}^{E_{\rm max}}\frac{dN}{dE}dE_{e^\pm}$) in this energy range is:

$$N_\pm \approx 9^{+6}_{-3} \times 10^{50}\left(\frac{E_{\rm min}}{1\,\mathrm{GeV}}\right)^{1-\alpha}\left(\frac{D_\gamma}{2\,\mathrm{kpc}}\right)^2. \quad (10)$$

3.2. Hadronic (π^0-decay) Model

We consider a spectrum $\frac{dN}{dE}$ of high-energy p^+ producing π^0 through collisions with low-energy p^+ in a molecular cloud of density $n_{\rm cloud}$. We model the high-energy p^+ particle spectrum $\frac{dN}{dE}$ with an exponentially cutoff power law:

$$\frac{dN}{dE} = A\left(\frac{E_{p^+}}{1\,\mathrm{TeV}}\right)^{-\alpha}\exp\left(\frac{-E_{p^+}}{E_{\rm cut}}\right)\ \mathrm{eV}^{-1}. \quad (11)$$

In this model $A \propto n_{\rm cloud}^{-1} D_\gamma^2$, which we fix at fiducial values $n_{\rm cloud} = 14\,\mathrm{cm}^{-3}$ (see Equation (4)) and $D_\gamma = 2$ kpc. The best fit parameters are listed in Table 2. We calculate the total p^+ energy W_{p^+} ($\equiv\int_{E_{\rm min}}^{E_{\rm max}} E_{p^+}\frac{dN}{dE}dE_{\rm p^+}$) by setting $E_{\rm min} = 1.22$ GeV, the dynamical threshold for π^0 production, and we set $E_{\rm max} = 10$ PeV (the `Naima` default value and $\gg E_{\rm cut}$). We find:

$$W_{p^+} = 1.4^{+0.2}_{-0.2} \times 10^{48}\left(\frac{n_{\rm cloud}}{14\,\mathrm{cm}^{-3}}\right)^{-1}\left(\frac{D_\gamma}{2\,\mathrm{kpc}}\right)^2\ \mathrm{erg}. \quad (12)$$

The 1σ errors in W_{p^+} were computed by Monte Carlo sampling

4. What Powers 1LHAASO J0500+4454?

1LHAASO J0500+4454's large radial extension $\theta_\gamma = 0.^\circ 41 \pm 0.^\circ 07$ rules out an extra-Galactic origin. Here we discuss three plausible Galactic origins for 1LHAASO J0500+4454: a molecular cloud (Section 4.1), a supernova remnant (Section 4.2), and an energetic outflow from a pulsar (Section 4.3). The plausibility of these scenarios depends on the energetics derived from SED modeling in Section 3 and also the locations of nearby MCs, SNRs, and pulsars (see Figure 1).

4.1. Molecular Cloud Scenario

If 1LHAASO J0500+4454 is powered by cosmic rays interacting with an MC, then there should be a sufficiently dense MC coincident with the observed γ-rays. The nearest known SNR to 1LHAASO J0500+4454 is HB9, and is therefore the most likely source of such cosmic rays. We will use W_{p^+} (Equation (12)) to calculate the energy budget of this hadronic scenario, assuming cosmic ray p^+ accelerated by SNR HB9 are powering 1LHAASO J0500+4454. This cosmic ray proton energy, currently with 1LHAASO J0500+4454 (W_{p^+}), and the projected distance from the center of 1LHAASO J0500+4454 to the center of HB9 imply a rate of energy injected from HB9 into cosmic ray p^+. The calculation of this energy injection rate indicates that the low upper limit on the molecular density in the 1LHAASO J0500+4454 region, combined with its projected distance from HB9, implies an unrealistic cosmic ray energy budget. This disfavors this hadronic scenario, and the details of these calculations are presented in Appendix A.

4.2. SNR Scenario

It is possible that 1LHAASO J0500+4454 is powered by particles accelerated to high energies in an SNR. Figure 1 shows that the only known nearby SNR HB9 does not overlap the 1LHAASO J0500+4454 emission region. However, a previously unknown SNR at this location could power 1LHAASO J0500+4454. The hypothetical SNR considered

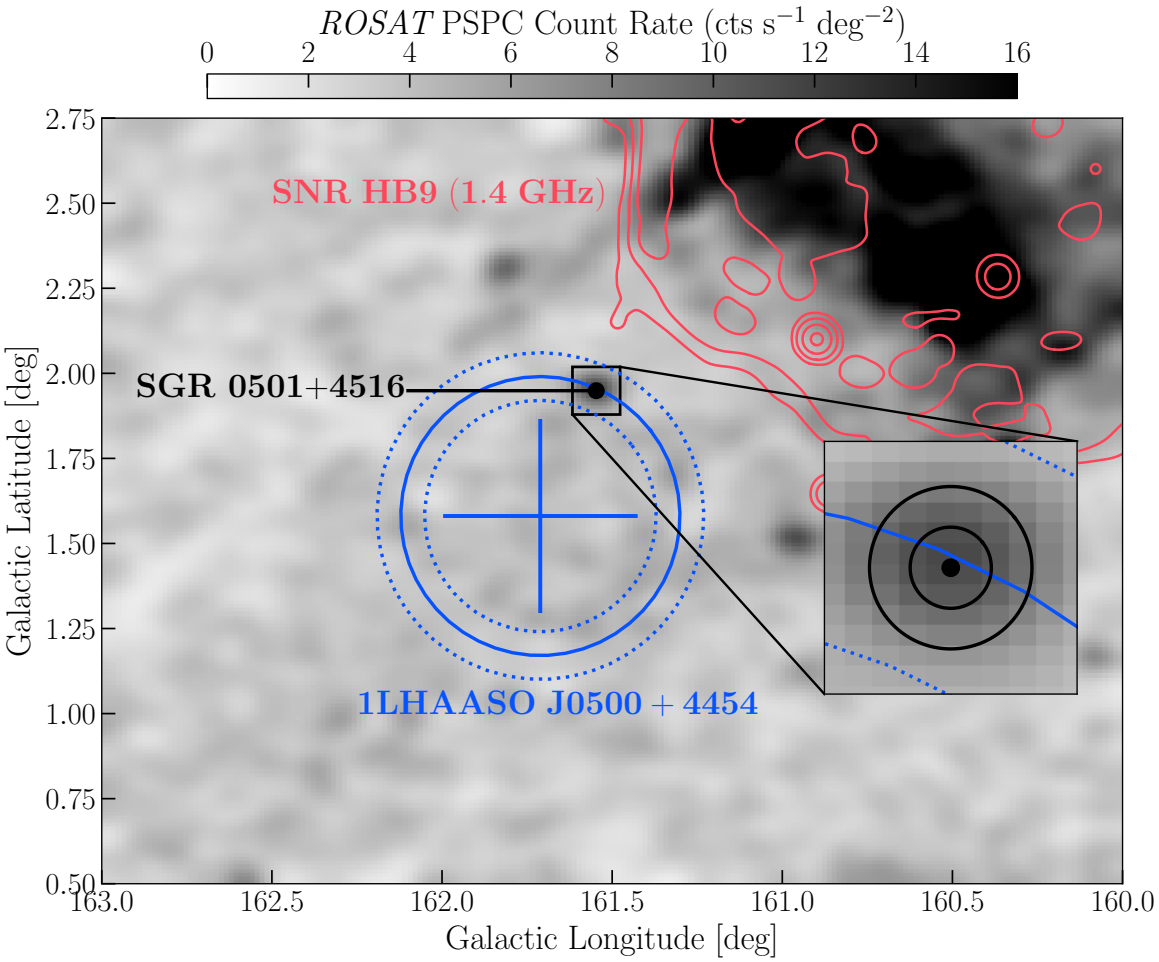

Figure 4. ROSAT PSPC observations of 1LHAASO J0500+4454 and the surrounding region. Red contours indicate the radio emission from SNR HB9. We have indicated the position of SGR 0501+4516, which is clearly detected by ROSAT at the edge of 1LHAASO J0500+4454. Inset: Circles around SGR 0501+4516 indicate its possible birth locations for pulsar ages $\tau_{\rm psr} = \tau_{\rm char}$ and $\tau_{\rm psr} = 2\tau_{\rm char}$ ($\tau_{\rm char} = 15$ kyr), and proper motion $\mu = 5.4$ mas yr^{-1}.

in this section is not assumed to be associated with any known astronomical objects in this field.

We list here the observed properties of 1LHAASO J0500+4454 that we will use to assess the plausibility of an SNR origin. First, we assume that the 1LHAASO J0500+4454 radius is greater than or equal to the SNR radius:

$$R_\gamma \gtrsim R_{\rm snr}. \tag{13}$$

Second, Figure 4 shows archival ROSAT All Sky Survey observations (ROR numbers 190568 and 190906) of 1LHAASO J0500+4454 and the surrounding region. Setting $n_{\rm H} \lesssim 5 \times 10^{21}\,{\rm cm}^{-2}$, a typical upper limit on the Galactic column density in this direction (HI4PI Collaboration et al. 2016), the ROSAT 3σ upper limit on the unabsorbed 0.1 −2.5 keV flux from the region with the same position and extension as 1LHAASO J0500+4454 is:

$$F_x \lesssim 1.0 \times 10^{-11}\,{\rm erg\,cm^{-2}\,s^{-1}}. \tag{14}$$

Third, we assume that the SNR has accelerated e^- to ∼40 TeV and accelerated p^+ to ∼70 TeV.

These constraints on the size, X-ray flux, and particle acceleration within the 1LHAASO J0500+4454 region pose significant challenges for the SNR origin scenarios, for an SNR at any evolutionary stage. The calculations demonstrating these challenges are presented in Appendix B.

4.3. Pulsar Scenario

A pulsar with an initial spin period P_0 and moment of inertia $I_{45} = 10^{45}\,{\rm g\,cm^2}$ has an initial rotational energy

$$E_{\rm rot} = 1.97 \times 10^{50}\quad I_{45}\quad \left(\frac{P_0}{10\ {\rm ms}}\right)^{-2}\quad {\rm erg}, \tag{15}$$

and an initial magnetic energy

$$E_{\rm B} = 1.66 \times \left(\frac{B_0}{10^{16}\,{\rm G}}\right)^2 \times 10^{49}{\rm erg}. \tag{16}$$

Equations (15) and (16) indicate that a sufficiently rapidly rotating and/or magnetized pulsar has an energy budget greater than the current 1LHAASO J0500+4454 leptonic energy $W_{e^\pm} \approx 3.8^{+2.7}_{-1.6} \times 10^{48}$ erg (Equation (9)). If $W_{e^\pm}$ originates from the initial rotational kinetic energy of the pulsar $E_{\rm rot}$ (Equation (15)), then $E_{\rm rot} > W_{e^\pm}$ requires an initial spin period $P_0 \lesssim 70$ ms. Likewise, if $W_{e^\pm}$ originates from the pulsar's initial magnetic energy, then $E_{\rm B} > W_{e^\pm}$ and Equation (16) requires internal magnetic field strength $B \gtrsim 5 \times 10^{15}$ G.

There are three known pulsars in the field of 1LHAASO J0500+4454 (Figure 1): PSR B0458+46, PSR J0454+4529, and the magnetar SGR 0501+4516. PSR B0458+46's distance was recently measured by FAST to be >2.7 kpc,

beyond the Perseus arm (W. C. Jing et al. 2023). At this distance, PSR B0458+46's $2.^{\circ}0$ angular separation from 1LHAASO J0500+4454 and the 30 kyr upper limit on the age of 1LHAASO J0500+4454 corresponds to a tangential velocity $v_{\perp} \gtrsim 3700\,\mathrm{km\,s^{-1}}$. Such a large velocity is highly unlikely, given the measured proper motions of young pulsars (G. Hobbs et al. 2005), and argues against an association with 1LHAASO J0500+4454.

PSR J0454+4529 has spin parameters $P \approx 1.39$ s and $\dot{P} \approx 4.89 \times 10^{-15}\,\mathrm{s\,s^{-1}}$ (C. M. Tan et al. 2020). If its true age $\tau_{\rm true}$ is comparable to its characteristic age $\tau_{\rm char} \equiv P/(2\dot{P}) \approx 4.5$ Myr, then it is too old to have powered 1LHAASO J0500+4454, whose age should be $\lesssim \tau_{\rm IC} \approx 30$ kyr in this scenario. If PSR J0454+4529's true age $\tau_{\rm true}$ is actually $\lesssim$30 kyr, then its initial spin period is comparable to its current spin period: $P_0 \approx P \approx 1.39$ s. Then its total spin-down energy since birth $E_{\rm sd} \approx \tau_{\rm true}\dot{E}_0 \lesssim (30\,\mathrm{kyr})(8 \times 10^{31}\,\mathrm{erg\,s^{-1}}) \approx 7.5 \times 10^{43}$ erg, which is $<< W_{e^{\pm}} \sim 4 \times 10^{48}$ erg (Equation (9)) and insufficient to power 1LHAASO J0500+4454.

Y.-L. Mong & C.-Y. Ng (2018) measured an upper limit on SGR 0501+4516's proper motion $\mu < 320\,\mathrm{mas\,yr^{-1}}$ (90% confidence level), which ruled out a proposed association with SNR HB9 (red contours in Figure 1). Recently, A. A. Chrimes et al. (2025) reported an Hubble Space Telescope-measured proper motion $\mu = 5.4 \pm 0.6\,\mathrm{mas\,yr^{-1}}$, consistent with SGR 0501+4516 being born within 1LHAASO J0500+4454's 95% positional uncertainty region (blue crosshairs in Figure 1). Black circles centered on SGR 0501+4516 in Figure 4 indicate radii of 15 kyr × 5.4 $\mathrm{mas\,yr^{-1}}$ and 30 kyr × 5.4 $\mathrm{mas\,yr^{-1}}$. SGR 0501+4516's offset from the center of 1LHAASO J0500+4454 is comparable to the offsets of other middle-aged (∼10 kyr) pulsars powering TeV pulsar wind nebulae (H. E. S. S. Collaboration et al. 2018).

Finally, SGR 0501+4516's 15 kyr characteristic age is consistent with the $\tau_{\rm IC} \approx 30$ kyr upper limit (see Equation (6)) on the age of the particles in 1LHAASO J0500+4454. Since both the position and age of SGR 0501+4516 are consistent with a source that could be powering 1LHAASO J0500+4454, we next consider the required energy budget.

5. Energy Budget of SGR 0501+4516

Here we calculate constraints on SGR 0501+4516's initial spin period P_0, assuming that its initial rotational energy dominates the input energy budget for 1LHAASO J0500+4454. 1LHAASO J0500+4454's total $e^{\pm}$ energy $W_{e^{\pm}} \approx 3.8^{+2.7}_{-1.6} \times 10^{48}$ erg (Equation (9)). The black curves in the left panel of Figure 5 show P_0 calculated for various values of the pulsar braking index n and spin-down timescale $\tau_{\rm sd}$, calculated with the standard spin-down formalism:

$$P = 5.76\,\mathrm{s} = P_0\left(1 + \frac{t}{\tau_{\rm sd}}\right)^{\frac{1}{n-1}}, \tag{17}$$

where we have set the time t equal to the pulsar's true age $\tau_{\rm true}$:

$$\tau_{\rm true} = \frac{2\tau_{\rm char}}{(n-1)} - \tau_{\rm sd}. \tag{18}$$

For the canonical dipole braking index value $n = 3$, the requirement that $P_0 \lesssim 70$ ms corresponds to $\tau_{\rm sd} \lesssim 10$ yr, with larger values of $\tau_{\rm sd}$ allowed for $n < 3$.

The above P_0 upper limit, calculated by setting $E_{\rm rot} > W_{e^{\pm}}$ is a hard upper bound on P_0, but energy losses would surely be significant over the lifetime of a pulsar wind nebula. A more realistic P_0 upper limit would account for these energy losses and require that $E_{\rm rot} > E_{\rm PWN}$, where $E_{\rm PWN}$ is the total energy injected into the $E_{\rm PWN}$ over its lifetime. We will calculate this upper bound on P_0 by setting $E_{\rm rot} > E_{\rm PWN}(t = \tau_{\rm sd})$, where $E_{\rm PWN}(t = \tau_{\rm sd})$ is the total PWN particle energy at time $t = \tau_{\rm sd}$. This is a conservative lower bound on $E_{\rm PWN}$ (upper bound on P_0), since according to standard pulsar spin-down formalism, most of the pulsar's rotational energy is injected between time $t = 0$ and time $t = \tau_{\rm sd}$:

$$\dot{E}(t) = \dot{E}_0\left(1 + \frac{t}{\tau_{\rm sd}}\right)^{-\frac{(n+1)}{(n-1)}}, \tag{19}$$

and we neglect energy injected after $t = \tau_{\rm sd}$.

We calculate $E_{\rm PWN}(t = \tau_{\rm sd})$ by accounting for adiabatic losses, which are expected to dominate the PWN energy budget at times $t > \tau_{\rm sd}$ (J. D. Gelfand et al. 2009). The energy of a relativistic ideal gas (adiabatic index $\gamma = 4/3$) in a spherical PWN bubble is inversely proportional to the PWN radius: $E_{\rm PWN} \propto R_{\rm PWN}^{-1}$. The observed size of 1LHAASO J0500+4454 gives the current PWN radius: $R_{\rm PWN}\,(t = \tau_{\rm true}) \approx 14.3$ pc. $R_{\rm PWN}(t = \tau_{\rm sd})$ can be calculated using the well-known self-similar PWN expansion law (R. A. Chevalier 1977; S. P. Reynolds & R. A. Chevalier 1984):

$$R_{\rm PWN} = 1.1\left(\frac{\dot{E}_0}{10^{38}\,\mathrm{erg\,s^{-1}}}\right)^{1/5}\left(\frac{t}{1\,\mathrm{kyr}}\right)^{6/5}\mathrm{pc}. \tag{20}$$

$R_{\rm PWN}$ depends weakly on the SNR explosion energy and ejecta mass ($R_{\rm PWN} \propto E_{\rm SN}^{3/10} M_{\rm ej}^{-1/2}$), which we have set to $E_{\rm SN} = 10^{51}$ erg and $M_{\rm ej} = 10\,M_{\odot}$ in Equation (20) above. We calculate $R_{\rm PWN}$ for the range of n and $\tau_{\rm sd}$ shown in the left panel of Figure 5. For each n and $\tau_{\rm sd}$ we calculate an expansion ratio

$$R_{\rm exp} \equiv \frac{R_{\rm PWN}(\tau_{\rm true})}{R_{\rm PWN}(\tau_{\rm sd})} \tag{21}$$

which we use to calculate

$$E_{\rm PWN}(\tau_{\rm sd}) = R_{\rm exp} \times E_{\rm PWN}(\tau_{\rm true}), \tag{22}$$

where $E_{\rm PWN}\,(\tau_{\rm true}) = W_{e^{\pm}}$ (Equation (9)).

For each $E_{\rm PWN}\,(\tau_{\rm sd})$, Equation (15) gives the corresponding P_0. Curves of constant P_0 calculated in this way are shown in blue in the left panel of Figure 5. The red curve in the right panel of Figure 5 indicates the n and $\tau_{\rm sd}$ values where P_0 calculated in the spin-down formalism (black in the left panel) and P_0 calculated from adiabatic losses (blue in the left panel) are consistent. The dark shaded regions in the right panel of Figure 5 indicate parameters that are ruled out by the requirements that $E_{\rm rot} > W_{e^{\pm}}$ and that 1LHAASO J0500+4454's age is $< \tau_{\rm IC}$ (Equation (6)). We find that a conservative accounting of adiabatic losses requires $P_0 \lesssim 5$ms. This conservative upper limit on P_0 neglects rotational energy injected after $t = \tau_{\rm SD}$, and the inevitable IC and synchrotron losses would push this upper limit even lower.

The calculations in this section used the fiducial $D_{\gamma} = 2$ kpc distance estimate. Since $R_{\rm PWN}\,(\tau_{\rm true}) \propto D$ (Equation (1)) and $W_{e^{\pm}} \propto D^{-1}$ (Equation (9)), the PWN energy $E_{\rm PWN}\,(\tau_{\rm sd}) \propto D^2$

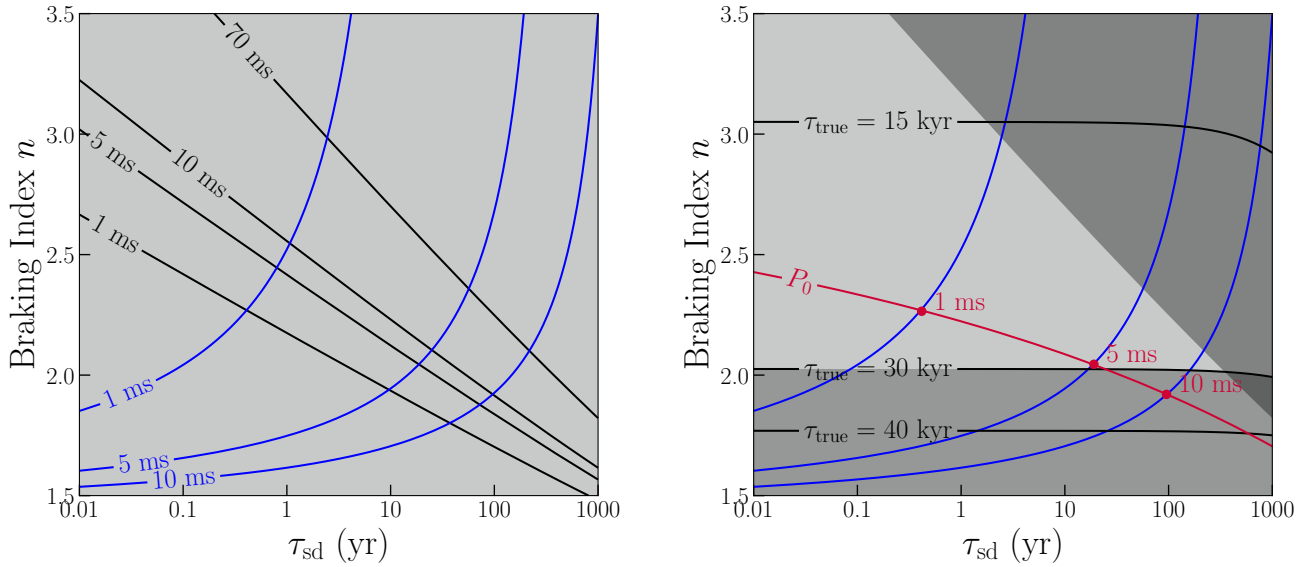

Figure 5. Left: SGR 0501+4516's initial spin period P_0 as a function of spin-down timescale $\tau_{\rm sd}$ and braking index n, calculated using two independent methods. The black lines indicate curves of constant P_0 calculated with standard spin-down formalism (Equation (17)), with SGR 0501+4516's currently measured $P = 5.76$ s and $\dot{P} = 5.9 \times 10^{-12}$ s s^{-1}. The blue lines trace curves of constant P_0 calculated using the currently measured particle energy in 1LHAASO J0500+4454 (Equation (9)) and accounting for adiabatic energy losses. Right: lines of constant pulsar true age $\tau_{\rm true}$ are indicated. $\tau_{\rm true} > 30$ kyr is ruled out by the half-life of ≈ 40 TeV $e^{\pm}$ inverse Compton scattering CMB photons (Equation (6)). The red curve indicates where the two P_0 calculations in the left panel are consistent.

and our derived initial spin period upper limits scale as $P_0 \propto D^{-1}$. P_0 also scales with the explosion energy and ejecta mass $P_0 \propto E_{\rm PWN}\,(\tau_{\rm true})^{-1/2} \propto R_{\rm PWN}\,(\tau_{\rm sd})^{1/2} \propto E_{\rm SN}^{3/20}$ and $P_0 \propto E_{\rm PWN}\,(\tau_{\rm true})^{-1/2} \propto R_{\rm PWN}\,(\tau_{\rm sd})^{1/2} \propto M_{\rm ej}^{-1/4}$. Finally, considering the above dependencies and the statistical uncertainty in $W_{e^{\pm}}$ (Equation (9)), we estimate

$$P_0 \lesssim 5^{+0.9}_{-2.5} \left(\frac{D_\gamma}{2\ \rm kpc}\right)^{-1} \left(\frac{M_{\rm ej}}{10\ M_\odot}\right)^{-1/4} \left(\frac{E_{\rm SN}}{10^{51}\ \rm erg}\right)^{3/20} \text{ms.} \quad (23)$$

6. Discussion

We consider magnetar SGR 0501+4516 the most likely candidate to power TeV source 1LHAASO J0500+4454, and follow-up observations and analysis can confirm this association. Confirmed magnetar TeV emission has remained elusive in part because magnetars are primarily located in crowded regions of the Galactic plane (S. A. Olausen & V. M. Kaspi 2014), where it is difficult to identify the origins of TeV emission from among many possible sources (molecular clouds, supernova remnants, and pulsars). XMM-Newton observations of magnetar Swift J1834.9−0846 indicate the presence of an X-ray PWN, but confirming its contribution to nearby TeV source HESS J1834−097 is complicated by the coincident SNR W41 and a candidate pulsar (XMMU J183435.3−084443) that could also be responsible for the TeV γ-rays (G. Younes et al. 2012, 2016). Similarly, the magnetar CXOU J171405.7−381031 in SNR CTB 37B is suspected to contribute to TeV source HESS J1713−381, but the surrounding SNR and nearby molecular clouds are also plausible sources of the observed TeV γ-rays (J. P. Halpern & E. V. Gotthelf 2010; E. V. Gotthelf et al. 2019). It is likewise unclear if the γ-ray source HESS J1808−204 is powered by the magnetar SGR 1806−20, the nearby massive stellar cluster, or a molecular cloud (H. E. S. S. Collaboration et al. 2018). This difficulty in identifying magnetar TeV emission is unfortunate because magnetar wind nebulae act as calorimeters, probing otherwise unobservable past magnetar activity.

6.1. *Magnetar* B *Fields, Initial Spin Periods, and* $P - \dot{P}$ *Evolution*

The origin of magnetar magnetic fields is not obvious, with various evidence both favoring and disfavoring the competing "fossil field" and dynamo generation hypotheses (H. C. Spruit 2008). R. C. Duncan & C. Thompson (1992) proposed that fast initial spin periods, $P_0 \sim 1$ ms, could generate magnetar-strength magnetic fields through a dynamo mechanism, and protoneutron star simulations also suggest that a convective dynamo can amplify neutron star dipole magnetic fields to 10^{15} G (C. J. White et al. 2022). However, J. Vink & L. Kuiper (2006) measured the forward shock radii r_s, ages τ, and interstellar medium (ISM) densities ρ of three SNRs hosting magnetars 1E 1841−045, 1E 2259+586, and SGR 0526−66. They calculated the explosion energies using the standard Sedov solution

$$R_s^5 = 2.026 \frac{E_{\rm SN}\,\tau^2}{\rho}, \quad (24)$$

and found typical SNR energies $E_{\rm SN} \sim 10^{51}$ erg. They concluded that if these three magnetars were born with $P_0 < 5$ ms, then most of the initial rotational energy seems not to have affected their surrounding SNRs.

Figure 6 shows SGR 0501+4516's possible trajectories (shaded gray) through the P–$\dot{P}$ diagram consistent with the constraints derived in Figure 5. These trajectories correspond to the red curve in the right panel of Figure 5, with $2.0 \lesssim n \lesssim 2.5$ and $\tau_{\rm SD} \lesssim 100$ yr, and SGR 0501+4516's spin-down measured dipole B field increasing over time. All P– $\dot{P}$trajectories pass close by the positions of PSR J1846−0258 in SNR Kes 75 and Swift J1834.9−0846, both

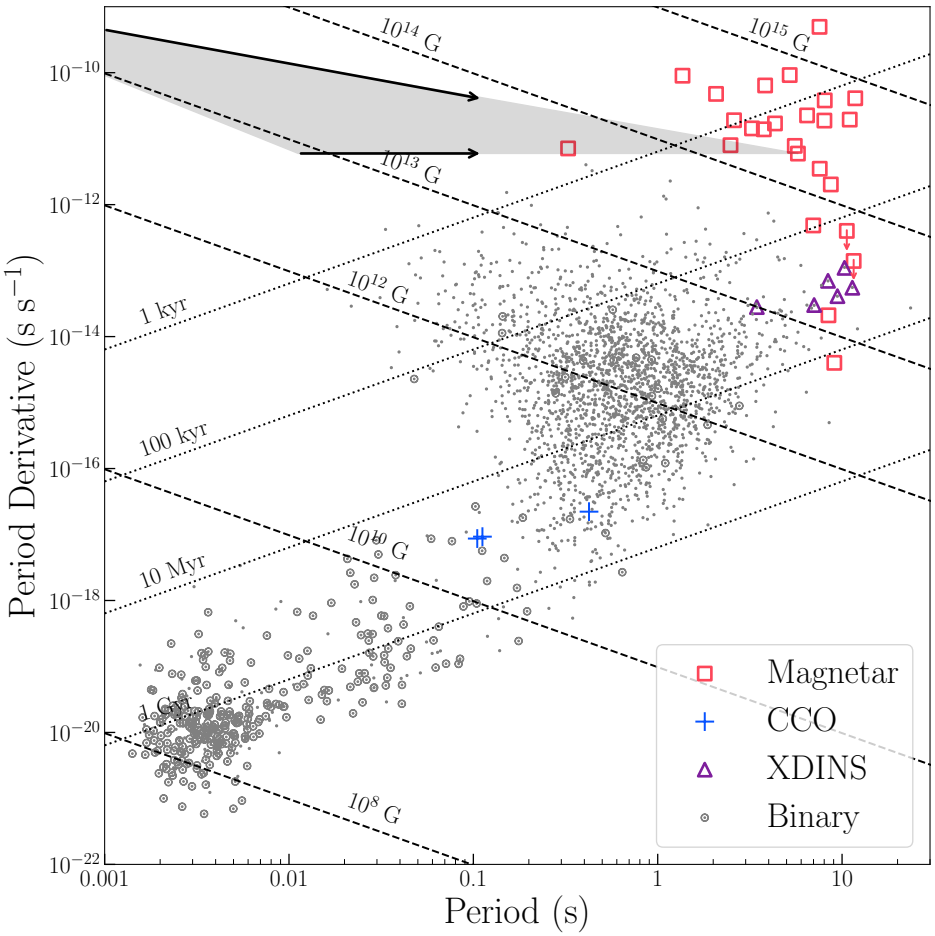

Figure 6. Evolution of SGR 0501+4516 through a $P - \dot{P}$ diagram if it was born with braking index $2.0 \lesssim n \lesssim 2.5$ and spin-down timescale $\tau_{\rm sd} \lesssim 100$ yr, as required by the energy budget constraints calculated in Section 5. Data are from the ATNF Pulsar Catalog version 2.1.1 (R. N. Manchester et al. 2005) and the McGill Online Magnetar Catalog (S. A. Olausen & V. M. Kaspi 2014).

magnetars with PWNe (E. V. Gotthelf et al. 2000; G. Younes et al. 2012, 2016). PSR J1846−0258's braking index has been measured to vary from $n = 2.65 \pm 0.01$ before an outburst to $n = 2.16 \pm 0.13$ postoutburst (M. A. Livingstone et al. 2011), indicating it is *currently* moving roughly parallel to the $P - \dot{P}$ trajectories indicated for SGR 0501+4516. Evidence of magnetar trajectories through the P–$\dot{P}$ diagram with $n < 3$ have been derived from proper motion measurements directed away from assumed birth locations in massive star clusters, with $n \sim 1.8$ for SGR 1806−20 and $n \sim 1.2$ for SGR 1900+14 (S. P. Tendulkar et al. 2012).

6.2. Directions for Future Work

JVLA radio follow-up observations can resolve, or place upper limits on, the synchrotron emission from the particles in 1LHAASO J0500+4454. This would further constrain the magnetic field strength and morphology of 1LHAASO J0500+4454, potentially providing further evidence that SGR 0501+4516 produced a TeV wind nebula by confirming that the magnetic field is low enough to be consistent with SGR 0501+4516's age. In the hard X-ray band, NuSTAR data can provide critical information about both the spatially resolved magnetic field strength within 1LHAASO J0500+4454 and also probe for spatial variations of the maximum $e^{\pm}$ energy throughout 1LHAASO J0500+4454.

7. Conclusion

We have presented evidence that the magnetar SGR 0501+4516 powers 1LHAASO J0500+4454. SGR 0501+4516's position, age, and energetics are consistent with this scenario. If SGR 0501+4516's rotational energy powers 1LHAASO J0500+4454, then it must have spun down rapidly ($\tau_{\rm sd} \lesssim 30$ yr) from a fast initial spin period: $P_0 \lesssim 5 \left(\frac{D_\gamma}{2\ \rm kpc}\right)^{-1}$ ms. This is consistent with theories that magnetar-strength magnetic fields originate from the rapid initial rotation of a protoneutron star. Follow-up observations and analysis at radio, X-ray, and γ-ray energies can confirm that SGR 0501+4516 powers 1LHAASO J0500+4454 and then further constrain the birth properties of SGR 0501+4516.

Acknowledgments

We thank Huirong Yan for helpful discussions on cosmic rays. J.A. would like to thank Jordan Eagle for helpful discussions regarding the Fermi Source Catalog and Fermi LAT data analysis. The research presented in this paper has used data from the Canadian Galactic Plane Survey, a Canadian project with international partners, supported by the Natural Sciences and Engineering Research Council.

Software: `astropy` (Astropy Collaboration et al. 2013, 2018), `matplotlib` (J. D. Hunter 2007), `xspec` (K. A. Arnaud 1996), `numpy` (C. R. Harris et al. 2020), `scipy` (P. Virtanen et al. 2020).

Appendix A
Molecular Cloud Scenario Calculations

The angular distance from the center of 1LHAASO J0500+4454 to the center of HB9 is $\theta_{\rm HB9} \approx 1.^{\circ}5$. The 1LHAASO J0500+4454 region has volume $V_\gamma \propto \theta_\gamma^3$. A spherical shell centered on HB9 with outer radius $\theta_{\rm HB9} + \theta_\gamma$ and inner radius $\theta_{\rm HB9} - \theta_\gamma$ has a volume $V_{\rm shell} \propto [(\theta_{\rm HB\,9} + \theta_\gamma)^3 - (\theta_{\rm HB\,9} - \theta_\gamma)^3]$ which implies $V_{\rm shell}/V_\gamma \approx 80$. The cosmic ray particle energy currently within the spherical shell centered on HB9 is then

$$W_{\rm shell} = W_{p^+}\left(\frac{V_{\rm shell}}{V_\gamma}\right) \approx 1.1^{+0.2}_{-0.2} \times 10^{50}\left(\frac{D_\gamma}{2\ {\rm kpc}}\right)^2 {\rm erg}. \quad \text{(A1)}$$

The cosmic ray crossing time $\tau_{\rm cross}$ from the inner radius to the outer radius of the shell is:

$$\tau_{\rm cross} \approx \frac{2R_\gamma}{c} \approx 94 \pm 16\left(\frac{D_\gamma}{2\ {\rm kpc}}\right){\rm yr}, \quad \text{(A2)}$$

which corresponds to power $\dot{E}_{p^+}$ injected into cosmic ray protons:

$$\dot{E}_p \equiv \frac{W_{\rm shell}}{\tau_{\rm cross}} \approx 3.8^{+1.2}_{-1.2} \times 10^{40}\left(\frac{D_\gamma}{2\ {\rm kpc}}\right){\rm erg\ s^{-1}}. \quad \text{(A3)}$$

A 0.7 ± 0.4 kpc distance to HB9 (S. Ranasinghe & D. Leahy 2022) and an age $\tau_{\rm snr} \sim 5$ kyr (D. A. Leahy & W. W. Tian 2007) implies that, if HB9 powers 1LHAASO J0500+4454, then over its lifetime HB9 injected energy $E_p \sim \dot{E}_p \tau_{\rm snr} \approx 2 \times 10^{51}$ erg into cosmic rays. This is an order of magnitude larger than HB9's estimated explosion energy $(1.5\text{–}3) \times 10^{50}$ erg (D. A. Leahy & W. W. Tian 2007), and disfavors a hadronic origin for 1LHAASO J0500+4454.

The LHAASO nondetection of SNR HB9 also disfavors a hadronic origin for 1LHAASO J0500+4454. If ~70 TeV p^+ are accelerated in HB9, then they should be accompanied by similar energy $e^\pm$. M. Araya (2014) found that Fermi observations of HB9 imply electron exponential cutoff energies ≈500 GeV in the IC scenario and proton exponential cutoff energies ≈80 GeV in the hadronic scenario. These exponential cutoffs in the particle spectra within HB9 in both the leptonic and hadronic scenarios are consistent with the LHAASO nondetection of HB9, and both cutoff energies are much lower than the $E_{\rm cut} \approx 70$ TeV inferred for 1LHAASO J0500+4454 (Table 2). This disfavors a hadronic origin for 1LHAASO J0500+4454.

Appendix B
SNR Scenario Calculations

The leptonic particle spectrum inferred from IC modeling of the 1LHAASO J0500+4454 SED (Table 2) would emit a higher synchrotron X-ray flux unless

$$B_{\rm snr} \lesssim 10\ \mu{\rm G} \quad \text{(leptonic case)}, \quad \text{(B1)}$$

assuming $D_\gamma = 2$ kpc and closer distances requiring smaller $B_{\rm snr}$. If 1LHAASO J0500+4454 is a previously unknown SNR accelerating protons up to at least ~70 TeV (see Table 2), then:

$$B_{\rm snr} \lesssim 35\ \mu{\rm G} \quad \text{(hadronic case)}, \quad \text{(B2)}$$

which we have calculated by assuming a cosmic ray proton to electron ratio $K_{\rm ep} = 0.01$. We will discuss both leptonic and hadronic scenarios, and consider an SNR currently in the free expansion or Sedov phase in Section B.1, and an SNR currently in the radiative phase in Section B.2.

B.1. SNR Scenario: Free Expansion or Sedov Phase

If 1LHAASO J0500+4454 is a previously unknown SNR accelerating electrons up to a maximum energy $E_{e,\rm max} \sim 40$ TeV, then either $E_{e,\rm max}$ is limited the SNR age, synchrotron losses or particle escape. If 1LHAASO J0500+4454 is a previously unknown SNR accelerating protons up to $E_{p,\rm max} \sim 70$ TeV, then either $E_{p,\rm max}$ is limited by either the SNR age or particle escape. S. P. Reynolds (1998) calculated the theoretical maximum particle energy in each of these scenarios:

$$E_{\rm max}({\rm TeV}) = \begin{cases} \eta^{-1}\, B_{10}\, V_{16}^2\, t_{250}, & \text{age limited} \\ \eta^{-1}\, B_{10}^{-1/2}\, V_{16}, & \text{loss limited} \\ B_{10}\, \lambda, & \text{escape limited} \end{cases} \quad \text{(B3)}$$

In the above equations, we have defined $t_{250} \equiv (t_{\rm SNR}/250\ {\rm yr})$, $V_{16} \equiv (V_{\rm s}/16000\ {\rm km\ s^{-1}})$, $B_{10} \equiv (B_{\rm SNR}/10\ \mu{\rm G})$, the maximum MHD wavelength is $\lambda \equiv (\lambda_{\rm max}/2.5 \times 10^{17}\ {\rm cm})$, and η is the ratio of the particle's mean free path to its gyroradius. The $B_{\rm SNR}$ dependence of the maximum energies, and our upper limit on $B_{\rm SNR}$ (Equations (B1) and (B2)), allow us to constrain the minimum required shock velocity in each case. A Sedov phase SNR must have a shock speed $V_{\rm s} \gtrsim 1.2 \times 10^4\ {\rm km\ s^{-1}}$, while a freely expanding SNR requires an even larger $V_{\rm s}$.

V_s corresponds to proton temperature (see, e.g., J. Vink (2012)):

$$kT_p \approx \frac{3}{16} m_p V_{\rm s}^2 \approx 196\ {\rm keV}\left(\frac{V_s}{10^4\ {\rm km\ s^{-1}}}\right)^2. \quad \text{(B4)}$$

The Coulomb equilibration timescale $\tau_{\rm ep}$ for the electrons to reach thermal equilibrium with the protons is (Y. B. Zeldovich & Y. P. Raizer 1966; H. Itoh 1984; J. Vink 2012):

$$\tau_{\rm ep} \approx 10\left(\frac{n_p}{1\ \ {\rm cm^{-3}}}\right)^{-1}\left(\frac{k\bar{T}}{1\ {\rm keV}}\right)^{3/2}\left(\frac{\ln\Lambda}{30.9}\right)^{-1} {\rm kyr}, \quad \text{(B5)}$$

where $n_{\rm p}$ is the proton density, the mean temperature $k\bar{T} \approx 0.6\, kT_p$, and $\ln\Lambda$ is the Coulomb logarithm:

$$\ln\Lambda = 30.9 - \ln\left[n_e^{1/2}\left(\frac{kT_e}{1\ {\rm keV}}\right)^{-1}\right]. \quad \text{(B6)}$$

For all $V_s \gtrsim 1.2 \times 10^4\ {\rm km\ s^{-1}}$, $\tau_{\rm ep}$ is much greater than a typical SNR age, so we cannot calculate the thermal X-ray emission from this hypothetical SNR by setting the electron temperature equal to $kT_{\rm SNR}$. (P. Ghavamian et al. 2007, 2013) We instead multiply kT_p by the electron to proton mass ratio to get a hard lower bound on the electron temperature:

$$kT_e \gtrsim \left(\frac{m_e}{m_p}\right) kT_{\rm p} \approx 107\ {\rm eV}\left(\frac{V_s}{1.2 \times 10^4\ {\rm km\ s^{-1}}}\right)^2. \quad \text{(B7)}$$

Observations of SNRs with shock velocities $V_s \gtrsim 400\ {\rm km\ s^{-1}}$ indicate $kT_e \gtrsim 0.3$ keV (P. Ghavamian et al. 2007, 2013), so Equation (B7) is probably unrealistically low, but we will

adopt it here for the most conservative X-ray flux calculation. We use the `apec` model available in `Xspec` to calculate the 0.1−2.5 keV flux from a thermal plasma with temperature $kT_e = 107$ eV (K. A. Arnaud 1996). The model normalization is:

$$N = \frac{10^{-14}}{4\pi R_\gamma^2} \int n_e n_{\rm H} dV \tag{B8}$$

and we have set $n_e = 1.2\, n_{\rm H}$ (assuming cosmic abundances) and $\int dV = \frac{4}{3}\pi R_\gamma^3$. We find that $n_e \lesssim 0.02\,{\rm cm}^{-3}$ is required to match the unabsorbed ROSAT X-ray flux upper limit F_x (Equation (14)). A Sedov phase SNR origin for 1LHAASO J0500+4454 is therefore ruled out by the archival ROSAT upper limits on its X-ray emission, as long as the SNR electron density $n_e \gtrsim 0.02\,{\rm cm}^{-3}$ (and a free expansion phase SNR would require an even lower n_e).

An SNR in the Sedov phase has radius $R_{\rm Sedov}$ (B. T. Draine 2011):

$$R_{\rm Sedov} = 5.0\ {\rm pc}\ E_{51}^{1/5} n_0^{-1/5} t_3^{2/5} \tag{B9}$$

and $V_{\rm Sedov}$:

$$V_{\rm Sedov} = 1950\ {\rm km\ s^{-1}}\ E_{51}^{1/5} n_0^{-1/5} t_3^{-3/5}. \tag{B10}$$

Requiring the Sedov shock velocity $V_{\rm Sedov} > 12{,}000\,{\rm km\,s^{-1}}$ at the beginning of the Sedov phase and also requiring $n_0 \lesssim 0.02\,{\rm cm}^{-3}$ implies that $E_{51} > 5$. This low-density environment and high explosion energy would be atypical.

B.2. SNR Scenario: Radiative Phase SNR

An SNR transitions from the Sedov phase to the radiative phase at time $t_{\rm rad}$ (J. M. Blondin et al. 1998; K. P. Dere et al. 2009; B. T. Draine 2011):

$$t_{\rm rad} = 49.3\ {\rm kyr}\ E_{51}^{0.22}\ n_0^{-0.55} \tag{B11}$$

$$\approx 13.9\ {\rm kyr}\ E_{51}^{0.22} \left(\frac{n_0}{10\ {\rm cm}^{-3}}\right)^{-0.55}, \tag{B12}$$

and the transition occurs at radius $R_{\rm rad}$:

$$R_{\rm rad} = 23.7\ {\rm pc}\ E_{51}^{0.29}\ n_0^{-0.42} \tag{B13}$$

$$\approx 9\ {\rm pc}\ E_{51}^{0.29} \left(\frac{n_0}{10\ {\rm cm}^{-3}}\right)^{-0.42}, \tag{B14}$$

when the SNR has a forward shock velocity $V_{\rm rad}$:

$$V_{\rm rad} = 188\ {\rm km\ s^{-1}}\ (E_{51}\, n_0^2)^{0.07} \tag{B15}$$

$$\approx 260\ {\rm km\ s^{-1}}\ E_{51}^{0.07} \left(\frac{n_0}{10\ {\rm cm}^{-3}}\right)^{0.14}. \tag{B16}$$

If 1LHAASO J0500+4454 is powered by an SNR that is currently in the radiative phase, the material behind the forward shock *might* have cooled enough that its thermal X-ray flux is below the ROSAT upper limit (Equation (14)).

If 1LHAASO J0500+4454 is associated with a radiative SNR, then the SNR must have had sufficiently fast shocks to accelerate electrons above ≈ 40 TeV in the past, and the SNR must have also reached the radiative phase before the electrons could cool below ≈40 TeV today. The magnetic field inside a radiative SNR is expected to at least exceed the typical ISM value, i.e., $B_{\rm snr} \gtrsim 2\,\mu$G, which implies the combined IC and synchrotron cooling timescale is $\lesssim$15 kyr. Setting $t_{\rm rad} < 15$ kyr in Equation (B11) requires:

$$E_{51}^{0.22} \left(\frac{n_0}{10\ {\rm cm}^{-3}}\right)^{-0.55} < 1.08. \tag{B17}$$

Since this leptonic radiative SNR scenario must invoke fast shocks, at least at the beginning of the Sedov phase, Equation (B10) requires:

$$E_{51}^{1/5} \left(\frac{n_0}{10\ {\rm cm}^{-3}}\right)^{-1/5} \gtrsim 2. \tag{B18}$$

For a typical explosion energy $E_{51} = 1$ the two equations above are equivalent to the contradictory requirements that $n_0 \gtrsim 9\,{\rm cm}^{-3}$ and $n_0 \lesssim 0.3\,{\rm cm}^{-3}$, and these two contradictory n_0 lower/upper limits differ by at least a factor of 7 for any $10^{-3} < E_{51} < 10$. This inconsistency disfavors a leptonic, radiative SNR origin for 1LHAASO J0500+4454.

Finally, we consider the possibility that 1LHAASO J0500+4454 is hadronic and associated with a currently radiative SNR. The diffusion coefficient for $E \sim 70$ TeV protons is:

$$\mathbb{D} = \mathbb{D}_0 \left(\frac{E}{1\ {\rm GeV}}\right)^{\delta} \tag{B19}$$

$$\approx 3 \times 10^{29}\ {\rm cm^2\ s^{-1}}, \tag{B20}$$

where we have set $\delta = 1/3$ (corresponding to a Kolmogorov spectrum of magnetic turbulence), and $\mathbb{D}_0 = 4 \times 10^{28}\,{\rm cm^2\,s^{-1}}$, a typical value in the Milky Way (A. W. Strong et al. 2007). The corresponding diffusion length l in a time t is:

$$l = \sqrt{4\mathbb{D}t} \tag{B21}$$

$$\approx 580 \left(\frac{t}{25\ {\rm kyr}}\right)^{0.5}\ {\rm pc}. \tag{B22}$$

This is a least ≈ 40 times larger than the observed 1LHAASO J0500+4454 radius R_γ for any distance $D_\gamma \leqslant 2$ kpc. We conclude that if 1LHAASO J0500+4454 is hadronic and powered by an SNR that is now radiative, then the local diffusion coefficient $\mathbb{D}_0 \lesssim 1.8 \times 10^{25}\,{\rm cm^2\,s^{-1}}$, at least three orders of magnitude lower than the typical value in the Milky Way.

In comparison, HAWC observations of the Geminga and Monogem pulsar halos indicate that the local diffusion coefficient for the 100 TeV $e^{\pm}$ in these regions is $4.5 \pm 1.2 \times 10^{27}\,{\rm cm^2\,s^{-1}}$, corresponding to $\mathbb{D}_0 \approx 2.2 \times 10^{26}\,{\rm cm^2\,s^{-1}}$ for $\delta = 1/3$ (A. U. Abeysekara et al. 2017). The Geminga and Monogem observations may indicate a $e^{\pm}$ diffusion coefficient around these PWNe that is lower than the typical value in the Milky Way, but these are observations of $e^{\pm}$, not protons. It is not clear if an even lower diffusion coefficient for protons propagating away from an old radiative SNR could be consistent with other observations of cosmic ray protons in the Milky Way, such as their inferred galactic escape timescale and isotropy.

ORCID iDs

J. A. J. Alford https://orcid.org/0000-0002-2312-8539
J. D. Gelfand https://orcid.org/0000-0003-4679-1058
M. Abdelmaguid https://orcid.org/0000-0002-4441-7081
P. Slane https://orcid.org/0000-0002-6986-6756

References

Abeysekara, A. U., Albert, A., Alfaro, R., et al. 2017, Sci, 358, 911
Ackermann, M., Ajello, M., Allafort, A., et al. 2013, Sci, 339, 807
Aharonian, F. A. 2013, APh, 43, 71
Araya, M. 2014, MNRAS, 444, 860
Arnaud, K. A. 1996, ASPC, 101, 17
Astropy Collaboration, Price-Whelan, A. M., Sipőcz, B. M., et al. 2018, AJ, 156, 123
Astropy Collaboration, Robitaille, T. P., Tollerud, E. J., et al. 2013, A&A, 558, A33
Ballet, J., Bruel, P., Burnett, T. H., et al. 2023, arXiv:2307.12546
Beloborodov, A. M., & Li, X. 2016, ApJ, 833, 261
Blondin, J. M., Wright, E. B., Borkowski, K. J., et al. 1998, ApJ, 500, 342
Bolatto, A. D., Wolfire, M., & Leroy, A. K. 2013, ARA&A, 51, 207
Camero, A., Papitto, A., Rea, N., et al. 2014, MNRAS, 438, 3291
Cao, Z., Aharonian, F., An, Q., et al. 2024, ApJS, 271, 25
Chevalier, R. A. 1977, in Supernovae, 66, 53, doi:10.1007/978-94-010-1229-4_5
Chrimes, A. A., Levan, A. J., Lyman, J. D., et al. 2025, A&A, 696, A127
Dame, T. M., & Thaddeus, P. 2022, ApJS, 262, 5
Dere, K. P., Landi, E., Young, P. R., et al. 2009, A&A, 498, 915
Draine, B. T. 2011, Physics of the Interstellar and Intergalactic Medium (Princeton Univ. Press)
Duncan, R. C., & Thompson, C. 1992, ApJL, 392, L9
Gelfand, J. D., Slane, P. O., & Zhang, W. 2009, ApJ, 703, 2051
Ghavamian, P., Laming, J. M., & Rakowski, C. E. 2007, ApJL, 654, L69
Ghavamian, P., Schwartz, S. J., Mitchell, J., et al. 2013, SSRv, 178, 633
Gotthelf, E. V., Halpern, J. P., Mori, K., et al. 2019, ApJ, 882, 173
Gotthelf, E. V., Vasisht, G., Boylan-Kolchin, M., et al. 2000, ApJL, 542, L37
Green, D. A. 2019, JApA, 40, 36
Green, D. A. 2025, JApA, 46, 14
Halpern, J. P., & Gotthelf, E. V. 2010, ApJ, 725, 1384
Harris, C. R., Millman, K. J., van der Walt, S. J., et al. 2020, Natur, 585, 357
H. E. S. S. Collaboration, Abdalla, H., Abramowski, A., et al. 2018, A&A, 612, A11
HI4PI Collaboration, Ben Bekhti, N., Flöer, L., et al. 2016, A&A, 594, 15
Hobbs, G., Lorimer, D. R., Lyne, A. G., et al. 2005, MNRAS, 360, 974
Hobbs, G., Lyne, A. G., Kramer, M., et al. 2004, MNRAS, 353, 1311
Hunter, J. D. 2007, CSE, 9, 90
Itoh, H. 1984, ApJ, 285, 601
Jing, W. C., Han, J. L., Hong, T., et al. 2023, MNRAS, 523, 4949
Kaspi, V. M., & Beloborodov, A. M. 2017, ARA&A, 55, 261
Leahy, D. A., & Tian, W. W. 2007, A&A, 461, 1013
Livingstone, M. A., Ng, C.-Y., Kaspi, V. M., et al. 2011, ApJ, 730, 66
Manchester, R. N., Hobbs, G. B., Teoh, A., et al. 2005, AJ, 129, 1993
Mong, Y.-L., & Ng, C.-Y. 2018, ApJ, 852, 86
Olausen, S. A., & Kaspi, V. M. 2014, ApJS, 212, 6
Ranasinghe, S., & Leahy, D. 2022, ApJ, 940, 63
Reynolds, S. P. 1998, ApJ, 493, 375
Reynolds, S. P., & Chevalier, R. A. 1984, ApJ, 278, 630
Rybicki, G. B., & Lightman, A. P. 1979, Radiative Processes in Astrophysics, 1979 (Wiley)
Spruit, H. C. 2008, AIPC, 983, 391
Strong, A. W., Moskalenko, I. V., & Ptuskin, V. S. 2007, ARNPS, 57, 285
Tan, C. M., Bassa, C. G., Cooper, S., et al. 2020, MNRAS, 492, 5878
Tendulkar, S. P., Cameron, P. B., & Kulkarni, S. R. 2012, ApJ, 761, 76
Thaddeus, P. 1977, IAUS, 75, 37
Vink, J. 2012, A&ARv, 20, 49
Vink, J., & Kuiper, L. 2006, MNRAS, 370, L14
Virtanen, P., Gommers, R., Oliphant, T. E., et al. 2020, NatMe, 17, 261
White, C. J., Burrows, A., Coleman, M. S. B., et al. 2022, ApJ, 926, 111
Xu, Y., Reid, M. J., Zheng, X. W., et al. 2006, Sci, 311, 54
Younes, G., Kouveliotou, C., Kargaltsev, O., et al. 2012, ApJ, 757, 39
Younes, G., Kouveliotou, C., Kargaltsev, O., et al. 2016, ApJ, 824, 138
Zabalza, V. 2015, ICRC, 34, 922
Zeldovich, Y. B., & Raizer, Y. P. 1966, in Elements of gasdynamics and the classical theory of shock waves, ed. W. D. Hayes & R. F. Probstein (Academic Press)